Tracing the magmatic/hydrothermal transition in regional low-strain zones: The role of magma dynamics in strain localization at pluton roof, implications for intrusion-related gold deposits

Eric Gloaguen[a,b,c*], Yannick Branquet[b,c,a], Alain Chauvet[d], Vincent Bouchot[a], Luc Barbanson[b,c,a] & J.L. Vigneresse[e]

[a] BRGM, ISTO, UMR 7327, BP 36009, F-45060 Orléans, France.
[b] Université d'Orléans, ISTO, UMR 7327, F-45071 Orléans,
[c] CNRS/INSU, ISTO, UMR 7327, F-45071 Orléans, France.
[d] Géosciences Montpellier, CNRS/INSU, UMR 5243, cc. 60, F-34095 Montpellier, France.
[e] Nancy-Université, CNRS/INSU, UMR 7566 G2R, BP 23, F-54501 Vandœuvre Cedex, France.

* Corresponding author: Tel: +33 2 38 64 34 21
Fax: +33 2 38 64 36 52
E-mail address: e.gloaguen@brgm.fr

Abstract

Structural controls are critical during magmatic-to-hydrothermal transition in the formation of intrusion-related gold deposits. They may explain why only some parts of intrusions are mineralized and why only very few intrusions host large deposits. Moreover, most of these gold deposits postdate peak regional metamorphism and were formed in zones of relatively low strain. Indeed, the efficiency of structural gold traps is highest along favourably oriented intrusion/host-rock contacts where mechanical instability maintains high permeability in the cracked thermal aureole. This may be reinforced by melt injections from an underlying root zone. We present a structural analysis of the deformation features of a granite-pluton roof; large-scale dykes and a network of gold veins are intensively developed in this roof, recording a succession of mechanical instabilities. Our gravity survey underlines the presence of a pluton feeder zone located just beneath the mineralized network. It is argued that interferences between regional stress and melt injection in the feeder zone favoured the development of the network by strain located close to the granite roof. This stresses the role of mechanical

instabilities triggered by the combined effects of regional stress and melt dynamics in determining the location and size of this type of gold deposit.

Keywords : magmatic-to-hydrothermal transition; pluton dynamics; strain localization; granite roof; mechanical instabilities; reduced intrusion-related gold deposit; Variscan; NW Spain; Boborás granite; Brués gold deposit

1. Introduction

Mechanical instabilities at the roof of a magmatic intrusion (the term ‘roof’ describes the apical envelope before erosion of an intrusion) appear to be a major structural prerequisite for localizing the magmatic-to-hydrothermal transition. Roof instabilities favour morphological features like cupolas, apexes and dyke swarms, which appear to be critical when mineralization is formed, as in the case of reduced intrusion-related gold deposits (e.g. Goldfarb et al., 2005; Hart, 2007). This class of gold deposit has only been recognized as a separate feature from the orogenic gold deposit class since 1999 and, as such, is in a juvenile state of understanding (Hart, 2007). Reduced intrusion-related gold deposits (RIRGD) include various deposit styles, such as skarns, disseminations, replacements, breccias, stockworks or, more commonly, intrusion-hosted sheeted arrays of thin quartz veins. Such veins with a low-sulphide Au-Bi-Te-W signature may develop within, beyond, or above the thermal aureole of the pluton. The intrusions have moderately low primary oxidation states, making them into reduced, ilmenite-series (Ishihara, 1981) granitoids. In such mineralized systems, the emplacement-to-cooling cycle of reduced felsic intrusions is assumed to be coeval and genetically related to gold deposition. RIRGD are therefore systems where the magmatic-to-hydrothermal transition is demonstrated by fluid-inclusion studies (Baker and Lang, 2001); they are generally centred on small plutons, plutonic apexes or dyke swarms, around which a cracked thermal aureole was developed (Baker and Lang, 2001; Stephens et al., 2004). Such intrusions are weakly deformed as they postdate regional ductile shearing and peak metamorphism. However, despite favourable conditions, to our knowledge no structural studies (including gravimetry) exist that are dedicated to such deposits, accounting for intrusion dynamics as structural controls of such magmatic-hydrothermal mineralized systems.

The magmatic-to-hydrothermal transition is a key process in ore-forming systems related to igneous activity (see review in Halter and Webster, 2004). While this transition is well known

from mineralogical and geochemical investigations, it remains difficult to assess via structural and textural analyses. This assertion is particularly valid for plutonic- and hydrothermal-related systems, as plutons emplaced close to high-strain regional shear zones (e.g. the footwall of detachments planes in metamorphic core complexes) may preserve magmatic and submagmatic textural gauges, but on-going high solid-state strain and rapid exhumation make it difficult accurately to establish a possible genetic link between magma injection and the subsequent hydrothermal system (e.g. Menant et al., 2013). In contrast, although magmatic and submagmatic textural gauges are subtle features due to low strain, plutons and their related ore-bearing systems emplaced far from major shear zones are good candidates for showing the magmatic-to-hydrothermal transition from a structural and textural point of view.

A weakly deformed magmatic system also provides an opportunity for evaluating the contribution of magma dynamics to the textural framework and plumbing system of a magmatic-to-hydrothermal transition.

In this paper we present a detailed structural and micro-structural analysis of the roof of the Late Variscan Boborás granite and its associated gold mineralization, the Brués deposit in northwestern Spain. The Boborás granite, dated at 318 ± 5 Ma (Gloaguen, 2006) is part of a roughly 30 km-long NNE-SSW alignment of four plutons, displaying a strong spatial association with gold mineralization located in and around the plutons (Fig. 1). Gold-bearing quartz veins in the granite, dykes or pegmatites, exhibit the typical low-sulphide Au-Bi-Te-W signature of RIRGD and contain locally magmatic brines. The Brués deposit on the north-western edge of the Boborás pluton is the most important deposit of the area (Asensio Pérez et al., 2000; Gloaguen et al., 2003; Gloaguen, 2006; Fig. 2). It is composed of a high density of near-parallel granite dykes and sills crosscutting micaschists at the roof of the pluton. Steeply-dipping dykes hosting gold-bearing quartz veins, trend N060°E close to the pluton and turn gradually to N100°E farther west. Veins from this deposit result from at least four successive deformation events with fluid infill. The deposition of gold and associated minerals occurred during the latest stages of the hydrothermal system. This network of dykes, sills and associated gold-bearing quartz veins is not observed elsewhere around the pluton.

We discuss the key parameters controlling fluid flow and mineral deposition, such as interaction between regional stress and pluton dynamics, the underlying root zone and anisotropy within the cracked thermal aureole. These parameters may explain why only some areas of the intrusion are mineralized, in other words why the mineralization does not cover the entire surface of the intrusion roof.

2. Geological setting

The Galician Variscan segment of the Ibero-Armorican orogenic belt (Fig. 1a) is composed of three major tectonic units (Ribeiro, 1974; Díez-Balda et al., 1990; Ribeiro et al., 1990a, 1990b) as a result of a long-lived and complex geological history (e.g. Martínez-Catalán et al., 2009). From base to top, we find (Fig. 1b): i) para-autochtonous schist and quartzite of the Schistose Domain of Galicia Trás-os-Montes (Ribeiro 1974; Marquínez García, 1984; Arenas et al., 1986; Farias et al., 1987; Farias Arquer, 1992); and ii) an allochthonous unit including the Ordenes complex, the main nappe complex of the Galician area (Martínez-Catalán et al., 2002; Ábalos et al, 2002). The region records three main deformation events, forming part of a long-lived Variscan history in response to subduction, continental collision and post-crustal-thickening extension (e.g. Matte, 1986; Lagarde et al., 1992; Martínez-Catalán et al., 2007, 2009). The study area (Fig. 1b) is mainly affected by ductile deformation events (D2, D3) and a D4 event, which largely overprint an earlier D1 event.

D2 is related to the emplacement of nappes expressed by a regional shallow-dipping cleavage and prograde metamorphism active between 345-320 Ma (Dallmeyer et al., 1997).

D3 corresponds to E-W horizontal compression (Díaz García, 1991; Gloaguen, 2006; Fernández et al., 2011) associated with north-verging detachments occurring between 330 and 315 Ma. D3 is characterized by large-scale upright folds and associated S3 axial cleavage, and by subvertical strike-slip shear zones (i.e. the Serra do Suido shear zone on Fig. 1b) (Martínez-Catalán et al., 1996). This event is also coeval with the emplacement of numerous granites. Four generations of plutons (G1 to G4; Capdevila and Floor, 1970), well constrained by crosscutting relationships (Fig. 1b), intrude the two abovementioned tectonic units that are mainly composed of micaschist, quartzite, feldspathic schist and paragneiss intercalations (Marquínez García, 1981, 1984; Farias et al., 1987; Pereira et al., 1993). G1 granodiorite is assumed to be coeval with D2 (Castro et al., 2002) whereas G2 (two-mica) and G3 (biotite-dominant) granites are syn-D3 (Barrera Morate et al., 1989; Farias Arquer, 1992). Finally, D4 is represented by the emplacement of large rounded G4 granodiorite plutons (e.g. the Ribadavia pluton; Figs. 1b and 2) that are related to generalized late-orogenic crustal extension (Aranguren et al., 2003). The emplacement of G4 plutons is estimated around 298 ± 2 Ma, the age of the neighbouring G4 Ourense pluton (Guttiérez-Alonso et al., 2011).

3. The Boborás granite

3.1 General features (Figs. 1 and 2)

The Boborás granite is a small north-south elongate elliptical intrusion (7 x 2.5 km) emplaced in the para-autochthonous unit consisting of monotonous micaschist including scarce dark quartzite and greywacke with numerous intercalations of quartz-segregation veins. A minimum emplacement depth of 9.3 km was estimated by means of fluid-inclusion studies on gold-bearing quartz veins (Gloaguen, 2006). It is a peraluminous S-type monzogranite containing no magnetite (average magnetic susceptibility of $53x10^{-6}$ S.I). The rock is homogeneous and has an equigranular texture where biotite is dominant over muscovite. The pluton does not seem to be deformed, and as a first approximation appears to be "strain free". Around the pluton, contact metamorphism is marked by andalusite commonly replaced by quartz and muscovite. At its southern edge, the Boborás granite is intruded by the post-D3, G4 Ribadavia pluton (Figs. 1b and 2).

3.2 Gravity and 3D geometry

A survey of 472 gravity measurements covered the Boborás granite area with a Lacoste & Romberg (G847) gravimeter (precision of ± 0.05 mGal). Elevations were determined using elevation benchmarks and a baro-altimeter with a precision of ± 0.5 m equivalent to ~0.1 mGal. The gravity data, referred to the Vigo international gravity station (n°105921 of the Bureau Gravimétrique International), were subjected to the classical corrections with a reduction density of 2.7. The kriging-interpolated contour map of the complete Bouguer anomaly (Fig. 3a) shows perturbations caused by the G2 and G3 plutons on a broad E-W negative gradient. The highest negative values to the east correspond to the large Carballiño G2 pluton. The regional anomaly was estimated by graphic smoothing of the Bouguer anomaly assuming broadly parallel regional isovalues (Fig. 3b), yielding a gently eastward-dipping plane with an estimated mean gradient of 0.78 mGal/km. The residual Bouguer anomaly was then calculated and its isovalues were contoured. Due to the large anomaly related to the Carballiño G2 granite, the 0 mGal contours around the small G3 plutons could not be obtained. In order to minimize this effect, a local regional anomaly was recalculated giving a closer approximation of the residual Bouger anomaly for the Boborás granite (Fig. 3c). The resulting data were used to perform a three-dimensional inversion (Cordell and Henderson, 1968; Vigneresse, 1990) based on a realistic density contrast of -0.03 between the granite and the hosting micaschist.

In the resulting depth-contour map (estimated error of ~15 %) and N-S section across the Boborás pluton (Fig. 3d), the pluton appears as a laccolith with a present-day mean thickness of 1-1.5 km, and with two probable feeder zones located close to the northern and southern

edges of the pluton. Between these feeders, the central zone of the pluton displays a swelling floor bordered by two thin zones shown by arrows on Fig. 3d. The eroded upper part of the pluton remains unknown, but, the residual-anomaly area being greater than the outcropping surface, it is likely that a significant part of the pluton remains below the present-day surface. In the Brués gold deposit area this assumption is strengthened by the very shallow dip (about 15° NW) of the granite-schist contact. The numerous occurrences of G3 pegmatite pods and dykes, generally concentrated at the top of intrusions, also attest to a nearby pluton roof (see London, 2008). Therefore, very little granite has been removed by erosion, and we can conclude that the present-day outcropping surface is close to the initial roof of the granite body.

3.3 Structures around the pluton

The micaschist is dominated by a nearly constant, N-S trending S2 cleavage with a mean dip of about 40° to the west (Fig. 2). Locally, S2 was intensively folded during D3, resulting in a near-horizontal N-S-trending L3 crenulation related to upright folds (Fig. 2). S3 cleavage trajectories are crosscut by the northern end of the pluton, clearly suggesting a discordant pluton (Fig. 2). Around the pluton, D3 is shown by: i) Boudin-like G2 aplite-pegmatite bodies deformed during roughly N-S stretching (Fig. 4a); ii) A sparse N-S, near-horizontal L3 lineation that developed in the thermal aureole where cordierite with rotated inclusion trails (Fig. 4b), and truncated andalusite-sillimanite porphyroblasts are observed (Fig. 4c), both indicate a top-to-the-north ductile shearing. Neither ductile detachments, nor high-strain mylonitic zones have been reported or recognized in the Boborás granite area (Fig. 2).

3.4 Dykes, sills and veins systems

Numerous sills, dykes and veins are exposed in the host micaschist around the Boborás granite. Structural, mineralogical and textural observations allow distinguishing four main types: G2 pegmatite and aplite; G3 granite dykes and sills; G3 pegmatite and aplite; and hydrothermal quartz veins.

(i) The most important network of intrusive sills and dykes is represented by pegmatite and aplite, varying in size from several metres to over a kilometre, and found all along the western border of the G2 Carballiño granite (only the most important bodies are shown on Fig. 2). Since they appear to be genetically associated to the G2 magmatism and are crosscut by G3 granite (Figs. 5b and 6a), they are labelled as G2 aplite-pegmatite and not further described.

(ii) Conversely, G3 sills and dykes are well-developed only northwest of the Boborás pluton

(Figs. 2 and 5a). Two groups of G3 granite injections into micaschist are defined: 1) G3 granite sills (Figs. 5b-d and 6c-d), and 2) high-angle north-dipping G3 granite dykes (Figs. 6b and c). The G3 granite sills are connected with numerous G3 high-angle granite dykes (Fig. 6c) with straight or irregular walls (Figs. 5b and d); some of them display a typical staircase geometry (Fig. 6b). The G3 dykes are connected to the Boborás pluton (Fig. 5b).

(iii) Several G3 pegmatites and/or aplites are observed in the Boborás granite, generally close to the roof. They are well represented mostly at the pluton border (e.g. the Xurenzas, Salon-Sobreido road stations on Fig. 2), and appear either as 10-cm-thick isolated vugs filled with coarse-grained pegmatite, or as 1 m-thick dykes of layered aplite-pegmatite.

The G3 granitic dykes are commonly bordered by centimetre to metre-scale quartz veins (Fig. 7a), either inside the dyke or along the dyke wallrock (Fig. 5c and d). At the Brués gold deposit (Figs. 2 and 5), the quartz veins can be sorted into extensional and sheared-extensional veins, hereafter called "shear veins". A few specific veins, filled with quartz and feldspar, correspond to hybrid shear-extensional fractures (Figs. 7e-f). Extensional veins are near-vertical (Fig. 2), commonly with an "en échelon" geometry consistent with a north-verging normal motion (Figs. 5c and 7c-d). The quartz in these veins is undeformed and milky to translucent in colour. The shear veins, however, have a laminated texture of alternating ~0.5 cm-thick ribbons of quartz and sulphide (Fig. 7b). At the Brués gold deposit, the shear veins exclusively occur along and inside the G3 dykes; they have steep northerly dips and their overall attitude and shear criteria demonstrate a north-verging normal motion (Figs. 7a and b).

At the pluton scale (Fig. 2), the extensional veins are preferentially concentrated along the north edge. Here, the magmatic G3 dykes and quartz veins gradually rotate from N060°E close to the pluton to N090°E farther west (Figs. 2 and 5a) and systematically dip to the north. The near-vertical extensional veins follow the same trend. Around the pluton, another type of shear vein is observed, corresponding to N120°E-trending left-lateral veins conjugated with N60°E-trending right-lateral veins (e.g. Fondo de Vila station on Fig. 2). These trends were also observed for the G3 pegmatites and aplites (Fig. 2), but the kinematics are often difficult to assess in such rocks. Right dihedral (Fig. 2) analysis of all shear veins measured around the Boborás pluton indicates that the vein pattern is compatible with a single stress tensor, implying horizontal E-W compression associated with horizontal N-S extension (Fig. 2).

4. Microfabrics in the Boborás pluton, dykes and sills

Structural observations on the Boborás G3 pluton, dykes and sills show little evidence of flow criteria. In the granite, a discreet sub-horizontal mineral lineation marked by N-S aligned elongate biotite is weakly developed at its roof. Under the microscope, submagmatic deformation features are characterized by numerous fractured plagioclases infilled by quartz and muscovite (Fig. 6e). The quartz inside the fractures is in continuity with that in the matrix, occasionally forming a single grain. Horizontal and north-south directed feldspar crystals are truncated, attesting to a local N-S extension (Fig. 6e). Numerous myrmekites are also observed at plagioclase/K-feldspar boundaries. In all these rocks, quartz forms large grains with little plastic deformation such as chessboard patterns, particularly abundant in the vicinity of the pluton roof (Fig. 6g). No evidence of overprinting deformation is observed, except in a few sectors where low- to medium-temperature dynamic recrystallization is seen. Incipient solid-state deformation in granite and dykes is attested by wavy extinction, twins and kink bands affecting biotite, muscovite and plagioclase (Fig. 6f), subgrains in quartz and some well-developed fractures affecting all granite-forming minerals and infilled with muscovite (Fig. 6h).

5. Microfabrics within hydrothermal veins

5.1 Vein infill succession

The three types of quartz veins (extensional, hybrid and shear veins) are composed of quartz, K-feldspar, apatite, muscovite-phengite and sulphides (Gloaguen, 2006). Veins are built-up with four generations of quartz, each one corresponding to a deformation stage. The first generation, Q1 (~70% of the vein infill) is commonly coeval with K-feldspar – muscovite ± apatite (Figs. 7e and f) and locally scheelite (Asencio Pérez et al., 2000). Q2 quartz can be elongate or euhedral - in overgrowth on Q1- and corresponds to the reopening of Q1 veins. Q2 quartz deposition was followed by the growth of masses of arsenopyrite crystals along the Q1 and Q2 grain boundaries. Subsequent deformation increments created spaces along quartz-arsenopyrite contacts or fractures inside the arsenopyrite crystals and are filled by Q3 quartz (Fig. 8a), often associated with pyrite and muscovite. This Q3 quartz locally is the matrix of brecciated borders of some shear veins. Finally, the last increment of deformation resulted in fractures and geodic cavities in arsenopyrite to be filled by undeformed and clear Q4 quartz grains (Fig. 8a), locally including electrum, Bi-Te sulphides and phengite.

5.2. Internal textures

Within the extensional veins, quartz is essentially of the Q1 type and occurs as large euhedral grains normal to vein walls. Abundant overgrowths are also observed. Some veins are geodic with centimetre-sized automorphic Q1 quartz crystals; they can contain magmatic brines as halite- and carbonates-bearing inclusions with a salinity of 35-40 wt. % NaCl equiv., which homogenize in the liquid phase at > 336° C (Gloaguen, 2006). Some extensional veins show single-phase sulphide domains composed of arsenopyrite (Fig. 7d).

A few hybrid veins, intermediate between tension and shear (Figs. 7e and f), display large euhedral quartz and K-feldspar grains, with a marked elongation oblique to the veins walls. The feldspars are commonly fractured parallel to the wall rock, suggesting a crack-seal growth mechanism (Ramsay, 1980). The central part of the vein is devoid of feldspar grains and presents thin fractures filled with white micas, and sulphide or oxide grains.

By contrast, quartz and arsenopyrite grains in shear veins are laminated and form irregular ribbons (Fig. 7b). Quartz grains define a N-S trending lineation that may be observed on the shear vein surfaces. The first quartz generation (Q1) forms elongate comb-grains whose long-axes are parallel or at a low angle to the vein walls. The quartz grains are highly deformed with features resulting from intense dynamic recrystallization (Fig. 8). Extinction is strongly wavy and high-angle conjugate shear bands are common in the Q1 grains (Figs. 8b-c and 9a-b). Small strain-free grains formed along the quartz grain boundaries and, inside the grains, along the conjugate shear bands (Figs. 8c, 8g and 9). Shearing may induce local rotation of Q1 quartz crystals or aggregates (Fig. 9a). Several vugs in deformed Q1 quartz are filled by euhedral Q2 quartz (Figs. 8j, 8k), attesting to the presence of micro pull-apart structures affecting Q1. However, Q2 mainly corresponds to very elongate grains parallel or oblique to the vein walls, between Q1 combs (Figs. 8c, 8i, 8g and 9b). Q2 quartz grains have far fewer fluid and solid inclusions than Q1 and are unaffected by dynamic recrystallization, having weak wavy extinction, no sub-grains and no conjugate shear bands. Locally, the elongate Q2 grains have parallel fluid-inclusion bands at an angle of 85 to 70° to the long grain axes (Figs. 8d and f). Some Q2 fibres have a very sharp boundary with neighbouring Q1 quartz (Fig. 8b), implying a different mode of crystallization.

5.3. Quartz [c]-axis fabrics from shear veins

Universal-stage measurements were made on quartz shear veins for both Q1 and elongate Q2 grains (Fig. 9), carefully avoiding several measurements on a single deformed comb grain. Measurements of long-axes of the Q1 and Q2 grain confirmed that they are parallel to the shear vein border (Fig. 9d and e), this parallelism being better defined for Q2 grains. The

average aspect ratio (length/thickness) is 8 for Q2 grains and only 4 for Q1 quartz. Most [c]-axes of the Q1 grains (Fig. 9d) lie close to the rim of the diagram, indicating a high-angle to the vein border. Such a distribution is generally observed in the case of comb quartz. Interestingly, many of the Q1 [c]-axes near the edge of the diagram are parallel to Q1 grain long-axes, indicating a Q1 grains rotation induced by normal shearing (Fig. 9a). Nevertheless, a second maximum is close to the center of the diagram and shows Q1 [c]-axes normal to the direction of shear.

The [c]-axis diagram of Q2 (Fig. 9e) is different and shows several [c]-axes close to the centre of the diagram. The four maxima of Q2 [c]-axes are at high angles with the grain long-axes, and mainly toward the local extension direction (north - X) with an angle of about 60° with the shear vein dip. These [c]-axis diagram differences between the two quartz generations suggest two different modes of nucleation that will be discussed in 6.3 below.

6. Interpretation

6.1. Granite emplacement during N-S stretching: associated magmatic to submagmatic strain gauges

According to our gravity data, the Boborás pluton is a small and thin elliptical laccolite. From these data, two main root zones are identified at the north and south ends of the pluton, suggesting that it was formed by the coalescence of intrusions ascending from these feeders (e.g. D'Eramo et al., 2006). The northern root zone is also attested by the high density of granite dykes and sills anywhere observed around the pluton. This may also have been the case for the southern root, but late crosscutting by the G4-pluton removed these features (Figs. 1 and 2). This may imply a N-S-directed magma flow of melts from each root, further suggested by the faint sub-horizontal mineral lineation marked by biotites at the pluton roof. The D3 E-W compression event led to N-S horizontal stretching marked by a N-S L3 stretching lineation (boudinaged G2 pegmatite and truncated andalusite and sillimanite in the thermal aureole, Figs. 4a and c), associated with top-to-the-north shearing (syntectonic cordierite porphyroblasts, Fig. 4b). At the Brués deposit, trends of G3 granite dykes are normal to the N-S stretching direction (Fig. 2), some having a staircase geometry (Fig. 6b). Such geometries suggest that the traps capturing the injected magma were coeval with a north-verging motion of the micaschist hanging-wall. This suggests that, at the end of D3, the top-to-the-north shearing locally evolved to a north-verging normal motion in specific areas like the edges of N-S-elongated plutons. This may partially explain the lack of S3-cleavage-

trajectory deflection at the north and south ends of the G3 plutons.

This north-verging normal motion persisted during magma crystallization as demonstrated by the truncated feldspars (Fig. 6e) considered to be markers of submagmatic deformation and melt relocation during the late stage of granite crystallization (e. g. Hibbard, 1987; Bouchez et al., 1992). The numerous myrmekites observed are considered to have been formed by Ca- and Na- replacement of K-feldspar during low-strain deformation in a sub-magmatic state (e.g. Simpson and Wintsch, 1989; Vernon, 2004).

6.2. High-temperature low-strain gauges

Deformation from the magmatic to solid-state condition is recorded by chessboard patterns (Fig. 6g) that are particularly abundant near the granite roof. Quartz chessboard patterns result from prism plus basal subgrain boundaries, revealing the activity of both ⟨a⟩ and prism ⟨c⟩-slip. The latter is restricted to the β-quartz stability field of high-temperature quartz and is thus dependant on P-T conditions (Mainprice et al., 1986; Kruhl, 1996, 1998). Plotting the minimum pressure obtained from fluid-inclusion studies (2.5 kbar; Gloaguen, 2006) in the P–T diagram given by Kruhl (1996), a minimum temperature of 630° C is needed for the formation of chessboard patterns in quartz in the Boborás granite within the β-quartz stability field. This provides strong evidence for subsequent deformation at subsolidus temperatures shortly after the beginning of crystallization (Kruhl, 1996, Stipp et al., 2002). Quartz grains with their irregular shapes, lobate boundaries, "pinning" features and large embayments are consistent with grain-boundary migration that calls for incipient dynamic recrystallization at high temperature and low strain rate (Jessell, 1987; Passchier and Trouw, 1996).

6.3. Fracturing during the magmatic-to-hydrothermal transition

During the final stages of granite roof crystallization, extensional and shear quartz veins begin to form close to granite dykes and the granite roof. The first Q1 quartz crystallized as comb quartz mainly normal to the vein walls but also parallel to them as shown by the [c]-axis diagram (Fig. 9). As we observed (Figs. 8 and 9), quartz with such orientation is a candidate for being affected by conjugate shear bands under subsequent shearing (van Daalen et al, 1999). The Q1 quartz is strongly deformed by normal shear and locally affected by grain rotation, now appearing as ribbons parallel to the vein borders with conjugate shear bands. Q2 quartz does not contain such bands and occurs within Q1 micro pull-apart structures as thin ribbons parallel to the vein border (Fig. 8). The quartz grain shapes, [c]-axis diagrams and crack-seal bands marked by fluid-inclusion bands are consistent with stripped bedding-Q2

veins formed in pull-apart cracks within Q1 quartz during normal shearing, which may correspond to bedding subparallel striping and opening of the Q1 shear veins (B-type of Koehn and Passchier, 2000; Bons et al., 2012), compatible with the north-verging normal faulting. This is coherent with local geodic (comb) Q2 quartz observed within deformed Q1 quartz (Figs. 8a, 8j and 8k). Because striped Q2 bedding veins form within Q1 quartz, they lack the typical inclusion trails and inclusion bands of host rock slices generally observed in such microstructures (Koehn and Passchier 2000). The differences between Q1 and Q2 aspect ratios, deformation and [c]-axis orientations are compatible with a Q2 crystallization postdating more deformed Q1, with Q2 crystallizing in cracks within Q1 during shearing. The growth of Q2 quartz may thus be syn-tectonic and polyphase veins infills also demonstrate a succession of deformation increments during the life of the hydrothermal system.

Consequently, we assume that the Boborás granite and its associated Brués gold deposit accurately record the magmatic-to-hydrothermal transition during a persistent and single low-strain (i.e. lack of mylonites and detachment planes) regional deformation. Hereafter, we will discuss the role of pluton dynamics (e.g. feeder zones, dykes, etc.) in the deformation localization process.

7. Discussion

7.1. Role of pluton dynamics in incremental strain localization

Combined with a low regional deformation intensity, we propose that the zone feeding the north edge of the pluton controlled the magmatic-hydrothermal system (Fig. 10). Successive magma injections through this feeder likely triggered mechanical instabilities along the northern contact of the pluton. Inflexions of the dyke trends, seen on Fig. 5a, suggest variations in stress orientation throughout the granite roof. The probable cause of such variations was interference between regional and magmatic stress fields, again underlining the role of pluton dynamics. The magmatic to solid-state microstructures observed in the granite roof record numerous deformation patterns that typically characterize successive mechanical instabilities during decreasing temperature (e.g. Pawley and Collins, 2002). The deformation continued after granite roof crystallization and became more localized, marked by quartz veins recording the magmatic-to-hydrothermal transition (e.g. Mustard, 2003).

7.2. Implication for reduced intrusion-related gold deposits (RIRGD)

The polyphase veins also exhibit a succession of deformation increments and fluids infills,

with the deposition of gold and associated minerals occurring at the end of the hydrothermal system life cycle. Since several stages of deformation and infill are required for creating an efficient trap for gold, such as fractured sulphide-bearing quartz veins acting as a electrochemical trap (e.g. Möller and Kersten, 1994), a succession of mechanical instabilities throughout the life of a hydrothermal system is required for efficient gold deposition.

The structural controls of RIRGD are considered "intermediate" between the strong variability of vein orientations in porphyries and the strong regularity of lode orientation in orogenic gold deposits (Stephens et al., 2004). These authors demonstrated the dominant control of regional stress fields without the involvement of major faults and large-scale shear zones, as in the case for orogenic gold deposits. Our results show that both pluton dynamics and favourably located magma-feeding zones have to be looked for in the exploration of such mineralized systems. In other words, the stages of pluton construction have to be carefully examined as they might control and located on-going mineralization and ore volume.

Eldursi et al. (2009) numerically modelled hydrothermal processes during pluton emplacement for the Boborás granite, according to which, favourable areas for mineralization are located along the upper edges and roof of the pluton. They also showed that highly permeable fractured thermal aureoles (10^{-15} m²) may restrict the mineralization in the upper corner of the Boborás pluton roof, and that mineral deposition can develop before and during the hottest phase of pluton emplacement. Our results agree with this hydrothermal modelling, particularly in explaining why only some parts of intrusion are mineralized. The mineralizing fluids were discharged and focused around high-permeability zones that are controlled by pluton dynamics, thus resulting in mechanical instabilities and strain localization.

8. Conclusions

Field and microstructural analysis of the Boborás granite, emplaced at a minimum depth of 9.3 km in a D3 E-W-directed shortening and N-S extension event, demonstrate that this thin laccolith (1-1.5 km) was emplaced at the end of D3. The regional D3 stress combined with magma inflow from the underlying root zone located a succession of mechanical instabilities in the northern part of the pluton roof. The Boborás pluton and its Brués gold deposit record a complete succession of magmatic and hydrothermal structures and textures, spanning the magmatic-to-hydrothermal transition during cooling of the pluton. Based on these data, we established a coherent model where gold mineralization is coeval with pluton emplacement,

magma dynamics and crystallization. Our results strongly argue for studying pluton dynamics and growth (e.g. locating feeder zones) when evaluating the structural controls of an intrusion-related gold deposit. For a long time, the interference between regional and pluton (volume-related) stress fields has been recognized as a major factor in pluton emplacement (Brun and Pons, 1981). In the same way, we suggest that such interference is critical for most ore deposits (Au, Sn, W) related to granite intrusions. Such "mineralizing" interference is favourably expressed in the case of regional low-strain zone. Conversely, such interference should play a minor role in ore formation when mineralizing granitic magma is emplaced in localized high-strain shear zones.

Acknowledgements

This study had the scientific and financial support from the CNRS and BRGM through the National Research Group on Ore Deposits (GDR n°2458, TRANSMET). We particularly thank J. Pons for constructive discussions. Our work also benefited from fruitful discussions with all co-workers of the research group involved in the GDR TRANSMET project. Constructive reviews by J.L. Bouchez, M. Tubía, an anonymous reviewer and S. Paterson (on a former version) helped in greatly improving the manuscript.

References

Ábalos, B., Carreras, J., Druguet, E., Escuder Viruete, J., Gómez Pugnaire, M.T., Lorenzo Álavarez, S., Quesada, C., Rodríguez Fernández, L.R., Gil Ibarguchi, J.I., 2002. Variscan and Pre-Variscan Tectonics. In: W. Gibbons and M.T. Moreno (Editors), The Geology of Spain. Geological Society, London, 155-183.

Aranguren, A., Cuevas, J., Tubía, J.M., Román-Berdiel, M.T., Casas-Sainz, A., Casas-Ponsati, A., 2003. Granite laccolith emplacement in the Iberian arc: AMS and gravity study of the La Trojiza pluton (NW Spain). Journal of the Geological Society, London 160, 435-445.

Arenas, R., Gil Ibarguchi, J.I., González Lodeiro, F., Klein, E., Martínez Catalán, J.R., Ortega Gironés, E., de Pablo Macía, J.G., Peinado, M., 1986. Tectonostratigraphic units in the complexes with mafic and related rocks of the NW of the Iberia. Hercynica II, 87-110.

Asensio Pérez, B., Pagés Valcarlos, J.L., Sierra López, J., González Del Tánago, J., 2000. Las mineralizaciones de oro asociadas al granite de Boborás (Brués, Orense). Gold mineralizations associated to the Boborás granito (Brués, Orense). Cuadernos Lab. Xeolóxico de Laxe, Coruña. 25, 87-89.

Baker, T., Lang, J.R., 2001. Fluid inclusion characteristics of intrusion-related gold mineralization, Tombstone-Tungsten magmatic belt, Yukon Territory Canada. Mineral Deposita 36, 563–582

Barrera Morate, J.L., Farias Arquer, P., González Lodeiro, F., Marquínez García, J.L., Martín Parra, L.M., Martínez Catalán, J.R., del Olmo Sanz, A., de Pablo Macía, J.G., 1989. Ourense/Verín. Mapa Geológico de España, 1/200000, 17/27, IGME, Madrid.

Bons, P.D., Elburg, M.A., Gomez-Rivas, E., 2012. A review of the formation of tectonic veins and their microstructures. Journal of Structural Geology 43, 33–62.

Bouchez, J.L., Delas, C., Gleizes, G., Nédélec, A., Cuney, M., 1992. Submagmatic microfractures in granites. Geology 20, 35-38.

Capdevila, R., Floor, P., 1970. Les différents types de granites hercyniens et leur distribution dans le nord ouest de l'Espagne. Boletín Geológico y Minero España, 81, 215-225.

Castro, A., Corretgé, G.L., De La Rosa, J., Enrique, P., Martínez, F.J., Pascual, E., Lago, M., Arranz, E., Galé, C., Fernández, C., Donaire, T., López, S., 2002. Palaeozoic Magmatism. In: Gibbons, W., Moreno, M.T. (Eds), The Geology of Spain. Geological Society, London, 117-153.

Cordell, L., Henderson, R.G., 1968. Iterative three dimensional solution of gravity anomaly using a digital computer. Geophysics 33, 596-601.

D'Eramo, F., Pinotti, L., Tubía, J.M., Vegas, N., Aranguren, A., Tejero, R., Gómez, D., 2006. Coalescence of lateral spreading magma ascending through dykes: a mechanism to form a granite canopy (El Hongo pluton, Sierras Pampeanas, Argentina). Journal of the Geological Society 163, 881–892.

Dallmeyer, R.D., Martínez Catalán, J.R., Arenas, R., Gil Ibarguchi, J.I., Gutiérrez Alonso, G., Farias, P., Aller, J., 1997. Diachronous Variscan tectonothermal activity in the NW Iberian Massif: Evidence from $^{40}Ar/^{39}Ar$ dating of regional fabrics. Tectonophysics 277, 307-337.

Díaz García, F., 1991. La estructura y la evolución metamórfica en un corte comprendido entre Carballiño y Forcarei. Area esquistosa de Galicia Central, NW de España. The structure and metamorphic evolution in a section between Carballiño and Forcarei. Schistose area of Central Galicia, NW of Spain. Cuadernos Lab. Xeolóxico de Laxe, Coruña.16, 273-299.

Díez Balda, M.A., Vegas, R., González Lodeiro, F., 1990. Autochthonous sequence. Structure. In: Dallmeyer, R.D., Martínez García, E. (Eds), Pre-Mesozoic Geology of Iberia. Springer-Verlag, Berlin, 172-188.

Eldursi, K., Branquet, Y., Guillou-Frottier, L., Marcoux, E., 2009. Numerical investigation of transient hydrothermal processes around intrusions: Heat-transfer and fluid-circulation controlled mineralization patterns. Earth and Planetary Science Letters 288, 70-83.

Farias, P., Gallastegui, G., González Lodeiro, F., Marquínez, J., Martín Parra, L.M., Martínez Catalán, J.R., de Pablo Macía, J.G., Rodríguez Fernández, L.R., 1987. Aportaciones al conocimiento de la litoestratigrafía y estructura de Galicia Central. Mem. Fac. Ciênc. Univ. Porto 1, 411-431.

Farias Arquer, P., 1992. El Paleozoico Inferior de la Zona de Galicia-Tràs-os-Montes (Cordillera Herciniana, NW de España). In: Gutiérrez Marco, J., Saavedra, J., Rábano, I. (Eds), Paleozoico Inferior de Ibero-América. University of Extremadura, Badajoz, 495-504.

Fernández, F.J., Díaz-García, F., Marquínez, J., 2011. Kinematics of the Forcarei Synform (NW Iberian Variscan Belt). In: Poblet, J. & Lisle, R.J. (Eds). Kinematic evolution and structural styles of fold-and-thrust belts. Geological Society, London, Special Publications 349, 185–201

Gloaguen, E., Chauvet, A., Branquet, Y., Gerbeaud, O., Ramboz, C., Bouchot, V., Lerouge, C., Monié, P., Cathelineau, M., Boiron, M.C., Marignac, C., Pourraz, N., Fourcade, S., Ruffet, G., Iglesias Ponce de León, M., 2003. Relations between Au / Sn-W mineralizations and late Variscan granite: Preliminary results from the Schistose Domain of Galicia-Trás-os-Montes Zone, Spain. In: Eliopoulos et al. (Eds), 7th biennial SGA meeting - Mineral Exploration and Sustainable Development, Athens, Greece, 1, 271-274.

Gloaguen, E., 2006. Apports d'une étude intégrée sur les relations entre granites et minéralisations filoniennes (Au et Sn-W) en contexte tardiorogénique (Chaîne Hercynienne, Galice centrale, Espagne). PhD thesis, Université d'Orléans, 572 p. http://tel.archives-ouvertes.fr/tel-00107391

Goldfarb, J.R., Baker, T., Dubé, B., Groves, D.I., Hart C.J.R., Gosselin, P., 2005. Distribution, Character, and Genesis of Gold Deposits in Metamorphic Terranes. Economic Geology 100th Anniversary volume, 407-450.

González Cuadra, P., Díaz García, F., Cuesta Fernández, A., 2006. Estructura del granito de Beariz (Ourense, Galicia). Structure of the Beariz granite (Ourense, Galicia). Geogaceta 40, 151–154.

Gutiérrez-Alonso, G., Fernández-Suárez, J., Jeffries, T.E., Johnston, S.T., Pastor-Galán, D. Brendan Murphy, J., Piedad Franco, M., Carlos Gonzalo, J., 2011. Diachronous post-orogenic magmatism within a developing orocline in Iberia, European Variscides. Tectonics 30, TC5008, doi:10.1029/2010TC002845.

Halter, W. E., Webster, J.D., 2004. The magmatic to hydrothermal transition and its bearing on ore-forming systems. Chemical Geology, 210, 1-6.

Hart, C.J.R., 2007. Reduced intrusion-related gold systems. In: Goodfellow, W.D., (ed.), Mineral deposits of Canada: A Synthesis of Major Deposit Types, District Metallogeny, the Evolution of Geological Provinces, and Exploration Methods: Geological Association of Canada, Mineral Deposits Division, Special Publication 5, 95-112.

Hibbard, M.J., 1987. Deformation of incompletely crystallized magma systems: granitic gneisses and their tectonic implications. The Journal of Geology 95, 543-561.

Ishihara, S., 1981. The granitoid series and mineralization. Economic Geology 75th Anniversary Volume, 458–484.

Jessell, M.W., 1987. Grain-boundary migration microstructures in a naturally deformed

quartzite. Journal of Structural Geology 9, 1007-1014.

Koehn, D., Passchier, C.W., 2000. Shear sense indicators in striped bedding-veins. Journal of Structural Geology 22, 1141-1151.

Kruhl, J.H., 1996. Prism- and basal-plane parallel subgrain boundaries in quartz: a micro-structural geothermobarometer. Journal of Metamorphic Geology 14, 581-589.

Kruhl, J.H., 1998. Prism- and basal-plane parallel subgrain boundaries in quartz: a microstructural geothermobarometer: Reply. Journal of Metamorphic Geology 16, 142-146.

Lagarde, J.L., Capdevila, R., Fourcade, S., 1992. Granites et collision continentale : l'exemple des granitoïdes carbonifères dans la chaîne hercynienne ouest-européenne. Bulletin de la Société Géologique de France 163, 597-610.

London, D. 2008. Pegmatites. The Canadian Mineralogist Special Publication 10, 347 p.

Mainprice, D.H., Bouchez, J.L., Blumenfeld, P., Tubía, J.M., 1986. Dominant c slip in naturally deformed quartz: implications for dramatic plastic softening at high temperature. Geology 14, 819-822.

Marquínez García, J.L., 1981. Estudio geológico del área esquistosa de Galicia Central (zona de Lalín-Forcarei-Beariz). Cuadernos Lab. Xeolóxico de Laxe, Coruña, 2, 135-154.

Marquínez García, J.L., 1984. La geología del área esquistosa de Galicia Central (Cordillera Herciniana, NW de Espana). Mem. Instituto Geológico y Minero de España, 213 p.

Martínez Catalán, J.R., Arenas, R., Díaz García, F., Pascual, F.J.R., Abati, J., Marquínez, J., 1996. Variscan exhumation of a subducted Palaeozoic continental margin, The basal units of the Ordenes Complex, Galicia, NW Spain. Tectonics 15, 106-121.

Martínez Catalán, J.R., Díaz García, F., Arenas, R., Abati, J., Castiñeiras, P., González Cuadra, P., Gómez Barreiro, J., Rubio Pascual, F.J., 2002. Thrust and detachment systems in the Ordenes Complex (northwestern Spain): Implications for the Variscan-Appalachian geodynamics. In: Martínez Catalán, J.R., Hatcher, R.D.J., Arenas, R., Díaz García, F. (Eds), Variscan-Appalachian dynamics: The building of the late Paleozoic basement. Geological Society of America, Boulder, Colorado, 163-182.

Martínez Catalán, J.R., Arenas, R., Díaz García, F., González Cuadra, P., Gómez-Barreiro, J., Abati, J., Castiñeiras, P., Fernández-Suárez, J., Sánchez Martínez, S., Andonaegui, P., González Clavijo, E., Díez Montes, A., Rubio Pascual, F.J., and Valle Aguado, B., 2007. Space and time in the tectonic evolution of the north-western Iberian Massif: Implications for the Variscan belt. In: Hatcher, R.D., Jr., Carlson, M.P., McBride, J.H.,

and Martínez Catalán, J.R. (eds). 4-D Framework of Continental Crust. Geological Society of America Memoir 200, 403–423, doi: 10.1130/2007.1200(21).

Martínez Catalán, J.R., Arenas, R., Abati, J., Sánchez Martínez, S., Díaz García, F., Fernández Suárez, J., González Cuadra, P., Castiñeiras, P., Gómez Barreiro, J., Díez Montes, A., González Clavijo, E., Rubio Pascual, F.J., Andonaegui, P., Jeffries, T.E., Alcock, J.E., Díez Fernández, R., López Carmona, A., 2009. A rootless suture and the loss of the roots of a mountain chain: The Variscan belt of NW Iberia. C.R. Geoscience 341, 114-126.

Matte, P., 1986. La chaîne varisque parmi les chaînes paléozoïques péri atlantiques, modèle d'évolution et position des grands blocs continentaux au Permo-Carbonifère. Bulletin de la Société Géologique de France 8, 9-24.

Menant, A., Jolivet, L., Augier, R., Skarpelis, N., 2013. The North Cycladic Detachment System and associated mineralization, Mykonos, Greece: Insights on the evolution of the Aegean domain. Tectonics 32, 433-452.

Möller P. and Kersten G., 1994. Electrochemical accumulation of visible gold on pyrite and arsenopyrite surfaces. Mineralium Deposita 29, 404–413.

Mustard, R., 2003. The magmatic-hydrothermal transition at Timbarra: Implications for the genesis of intrusion-related gold deposits. In: Eliopoulos et al. (Eds), 7th biennial SGA meeting - Mineral exploration and sustainable development, Athens, Greece, 1, 355-358.

Passchier, C.W., Trouw, R.A.J., 1996. Microtectonics. Springer-Verlag, Berlin, 289 p.

Pawley, M.J., Collins, W.J., 2002. The development of contrasting structures during the cooling and crystallisation of a syn-kinematic pluton. Journal of Structural Geology 24, 469-483.

Pereira, E., Ribeiro, A., Meireles, C., 1993. Cisalhamentos hercínicos e controlo das mineralizações de Sn-W, Au e U na Zona Centro-Ibérica, em Portugal. Cuadernos Lab. Xeolóxico de Laxe, Coruña,18, 89-119.

Ramsay, J.G., 1980. The crack–seal mechanism of rock deformation. Nature 284, 135–139.

Ribeiro, A., 1974. Contribution à l'étude tectonique de Trás-os-Montes oriental. Memórias dos Serviços Geológicos de Portugal 24, 168 p.

Ribeiro, A., Pereira, E., Dias, R., 1990a. Allochthonous sequences. Structure in the Northwest of the Iberian Peninsula. In: Dallmeyer, R.D., Martínez Garcia, E. (Eds), Pre-Mesozoic geology of Iberia. Springer-Verlag, Berlin Heidelberg, 220-236.

Ribeiro, A., Quesada, C., Dallmeyer, R.D., 1990b. Geodynamics evolution of the Iberian Massif. In: Dallmeyer, R.D., Martínez García, E. (Eds), Pre-Mesozoic Geology of Iberia. Springer-Verlag, Berlin Heidelberg, 399-409.

Simpson, C., Wintsch, R.P., 1989. Evidence for deformation-induced K-feldspar replacement by myrmekite. Journal of Metamorphic Geology 7, 261-275.

Sizaret, S., Branquet, Y., Gloaguen, E., Chauvet, A., Barbanson, L., Arbaret, L., Chen, Y., 2009. Estimating the Local Paleo-fluid Flow Velocity: New Textural Method and Application to Metasomatism. Earth and Planetary Science Letters 280, 71–82.

Stephens, J.R., Mair, J.L., Oliver, N.H.S., Hart, C.J.R., Baker, T., 2004. Structural and mechanical controls on intrusion-related deposits of the Tombstone Gold Belt, Yukon, Canada, with comparisons to other vein-hosted ore-deposit types. Journal of Structural Geology 26, 1025-1041.

Stipp, M., Stünitz, H., Heilbronner, R., Schmid, S.M., 2002. The eastern Tonale fault zone: a "natural laboratory" for crystal plastic deformation of quartz over a temperature range from 250 to 700°C. Journal of Structural Geology 24, 1861-1884.

van Daalen, M., Heilbronner, R., Kunze, K., 1999. Orientation analysis of localized shear deformation in quartz fibres at the brittle-ductile transition. Tectonophysics 303, 83-107.

Vernon, R.H., 2004. A Practical Guide to Rock Microstructures. Cambridge University Press, Cambridge, United Kingdom, 606 p.

Vigneresse, J.L., 1990. Use and misuse of geophysical data to determine the shape at depth of granitic intrusions. Geological Journal 25, 249-260.

Figure captions

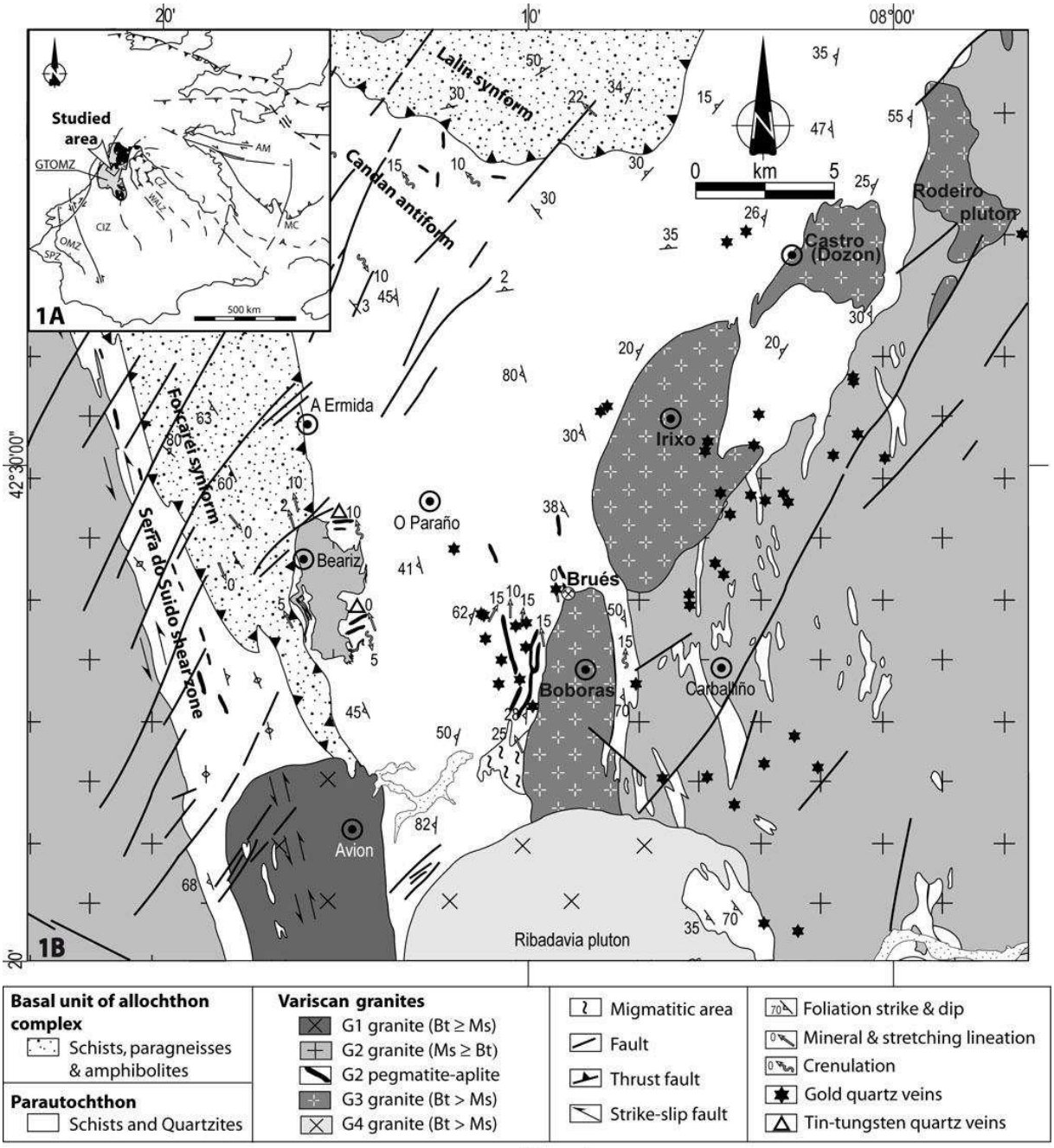

Figure 1

Fig. 1: The study area in the western part of the Variscan belt before opening of the Bay of Biscay. (A) Location in Western Europe; abbreviations: AM, Armorican Massif, MC, Massif Central, CZ, Cantabrian Zone, WALZ, West-Asturian-Leonese Zone, GTOMZ, Galicia-Trás-os-Montes Zone, CIZ, Centro Iberian Zone, OMZ, Ossa-Morena Zone, SPZ, South Portuguese Zone; (B) Geological sketch map of the Schistose Domain in Galicia Trás-os-Montes Zone (modified from Barrera Morate et al, 1989, and from González Cuadra et al., 2006 and Sizaret et al., 2009 for the Beariz granite).

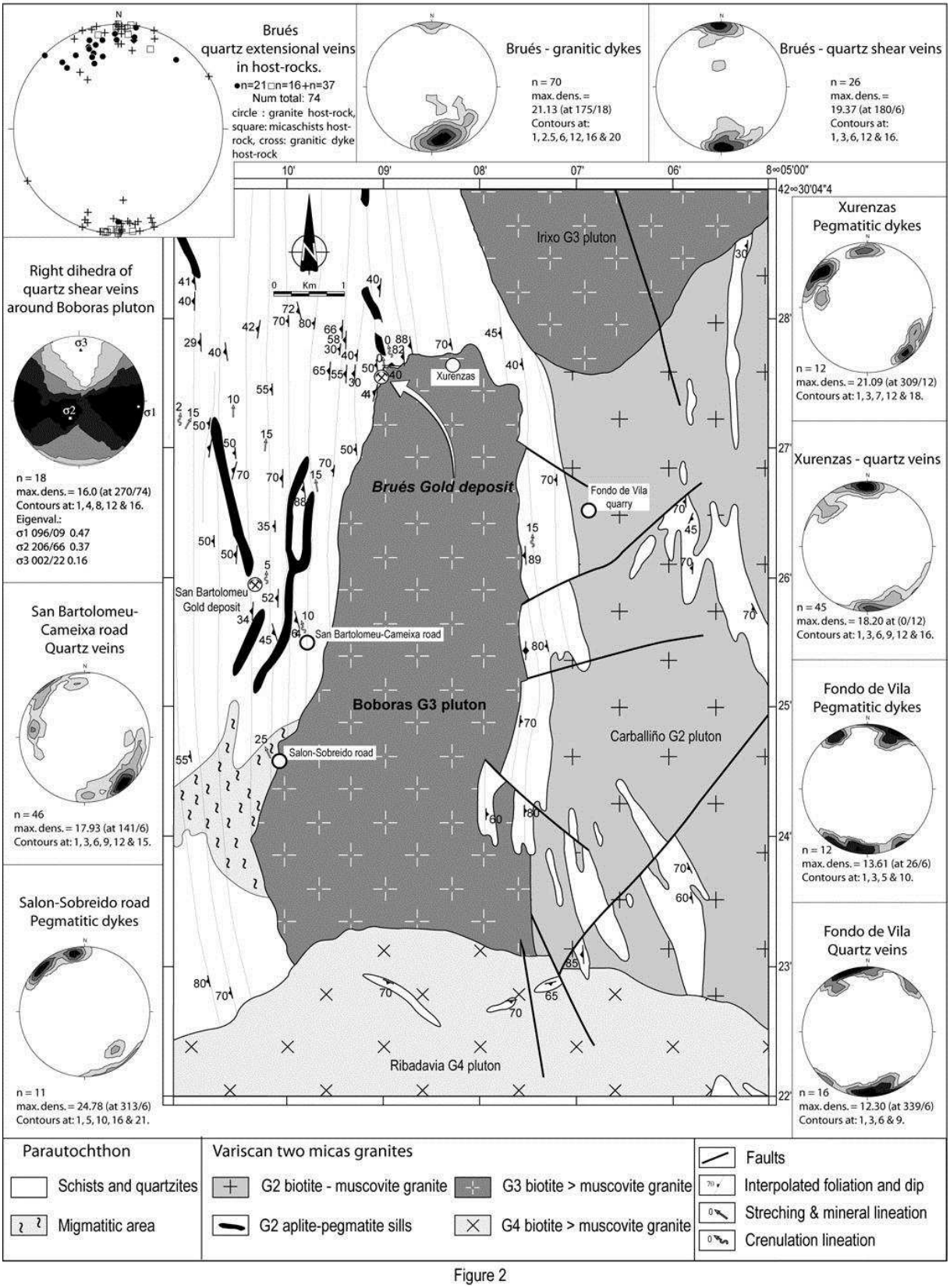
Brués
quartz extensional veins
in host-rocks.
●n=21□n=16+n=37
Num total: 74
circle : granite host-rock,
square: micaschists host-
rock, cross: granitic dyke
host-rock
Brués - granitic dykes
n = 70
max. dens. =
21.13 (at 175/18)
Contours at:
1, 2.5, 6, 12, 16 & 20
Brués - quartz shear veins
n = 26
max. dens. =
19.37 (at 180/6)
Contours at:
1, 3, 6, 12 & 16.
10'
09'
08'
07'
06'
8∞05'00"
42∞30'04"4
Right dihedra of
quartz shear veins
around Boboras pluton
σ1
σ2
σ3
n = 18
max. dens. = 16.0 (at 270/74)
Contours at: 1, 4, 8, 12 & 16.
Eigenval.:
σ1 096/09 0.47
σ2 206/66 0.37
σ3 002/22 0.16
Irixo G3 pluton
Xurenzas
Brués Gold deposit
Fondo de Vila
quarry
San Bartolomeu
Gold deposit
San Bartolomeu-Cameixa road
Boboras G3 pluton
Carballiño G2 pluton
Salon-Sobreido road
Ribadavia G4 pluton
0 Km 1
Xurenzas
Pegmatitic dykes
n = 12
max. dens. = 21.09 (at 309/12)
Contours at: 1, 3, 7, 12 & 18.
Xurenzas - quartz veins
n = 45
max. dens. = 18.20 at (0/12)
Contours at: 1, 3, 6, 9, 12 & 16.
Fondo de Vila
Pegmatitic dykes
n = 12
max. dens. = 13.61 (at 26/6)
Contours at: 1, 3, 5 & 10.
Fondo de Vila
Quartz veins
n = 16
max. dens. = 12.30 (at 339/6)
Contours at: 1, 3, 6 & 9.
San Bartolomeu-
Cameixa road
Quartz veins
n = 46
max. dens. = 17.93 (at 141/6)
Contours at: 1, 3, 6, 9, 12 & 15.
Salon-Sobreido road
Pegmatitic dykes
n = 11
max. dens. = 24.78 (at 313/6)
Contours at: 1, 5, 10, 16 & 21.
Parautochthon
Schists and quartzites
Migmatitic area
Variscan two micas granites
G2 biotite - muscovite granite
G3 biotite > muscovite granite
G2 aplite-pegmatite sills
G4 biotite > muscovite granite
Faults
Interpolated foliation and dip
Streching & mineral lineation
Crenulation lineation

Figure 2

Fig. 2: Geological map of the Boborás granite area (modified from the 1:50,000-scale Ourense sheet 187 and the 1:200,000-scale Oursense/Verin sheet 17/27 of the Geological map of Spain, and field work by Gloaguen, 2006). Orientation diagrams (lower hemisphere, equal area) of G3 Boborás granite dykes, quartz veins and G3 aplite-pegmatite dykes around the Boborás pluton are indicated.

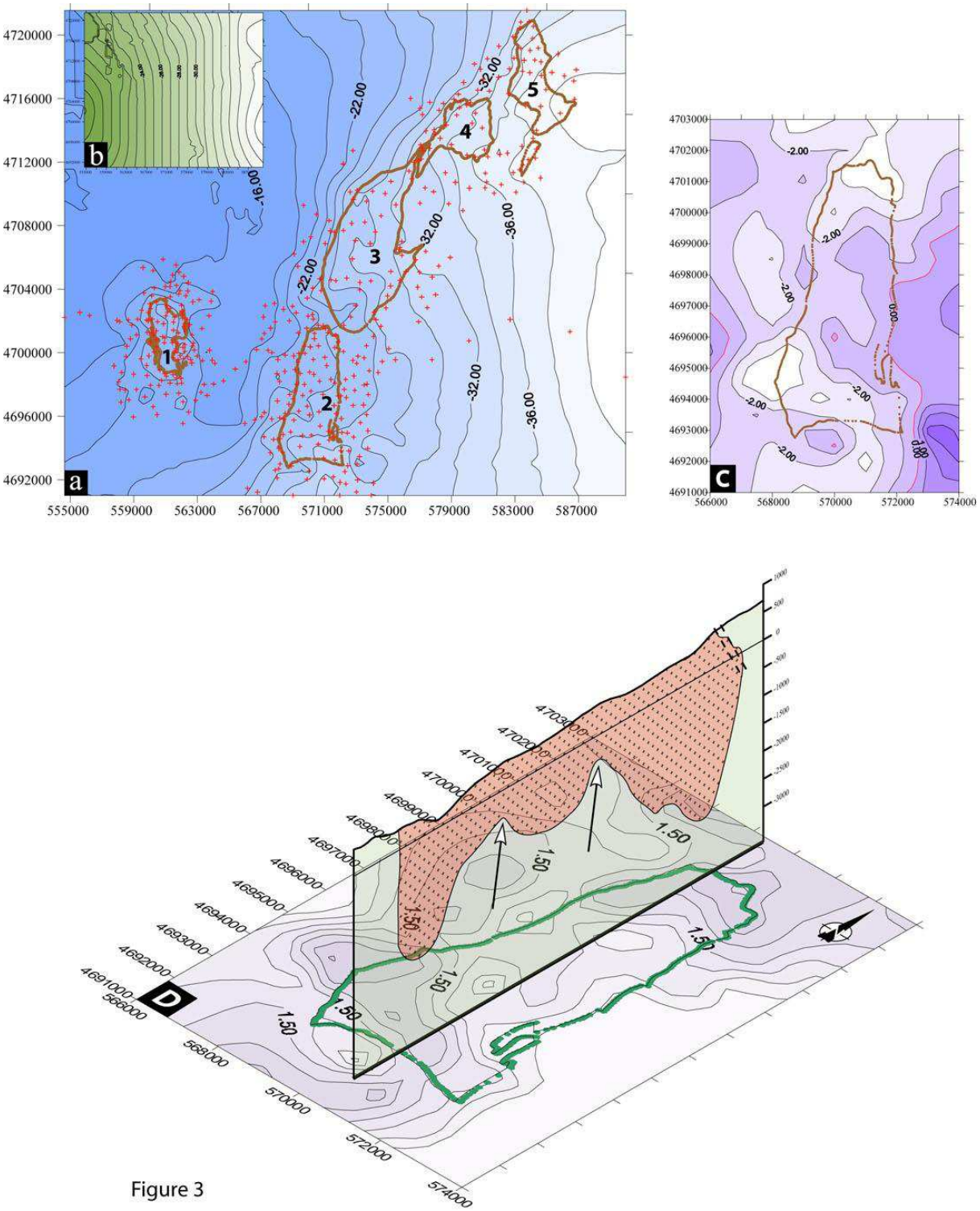

Figure 3

Fig. 3: Geometry of the Boborás granite. All maps have ED50 metric coordinates (Hayford 1924 Ellipsoïd, European Datum 1950, UTM 29N). (a) Complete Bouguer anomaly map of the area (mGal). Surface contours of small plutons are labelled. G2 granites: Beariz (1), and G3 granites: Boborás (2), Irixio (3), Castro Dozón (4), Rodeiro (5). East of the G3 pluton alignment, the large and massive Carballiño G2 granite (not shown, see Fig. 2) has a major effect on the Bouger anomaly. (b) Regional anomaly (mGal) calculated for the study area. (c) Residual Bouguer anomaly for the Boborás granite (mGal); although the 0 mGal isovalue is not closed, two root zones may be identified at the north and south edges of the pluton. (d) Depth-contour map (km) and interpretative cross-section of the Boborás granite after inversion using a 0.03 density contrast.

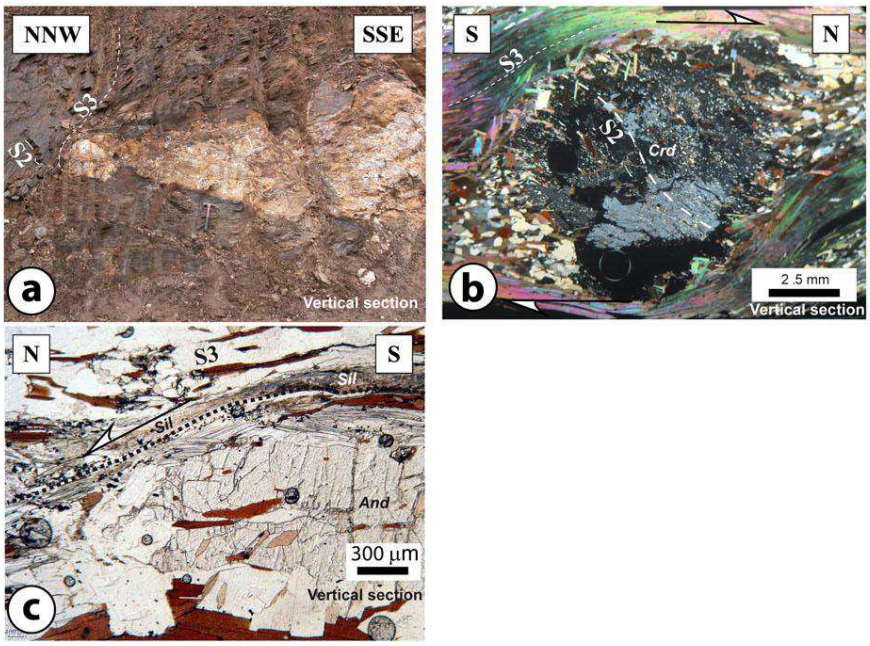

Figure 4

Fig. 4: Photographs of outcrops and microstructures indicating deformation kinematics in host-micaschists during D3. (a) Boudin-like layered aplite-pegmatite related to G2 granite; the near-vertical S3 crenulation cleavage turns around the magmatic body (Hammer for scale). (b)

Syntectonic cordierite porphyroblast within micaschist of the metamorphic aureole; inclusion trends in the centre show about 45° dextral rotation of the blast with respect to S3; this is compatible with a D3 top-to-the-north shearing also indicated by asymmetric strain shadows. (c) Truncated horizontal N-S trending andalusite crystal associated with small sillimanite-bearing D3 shear band.

Figure 5

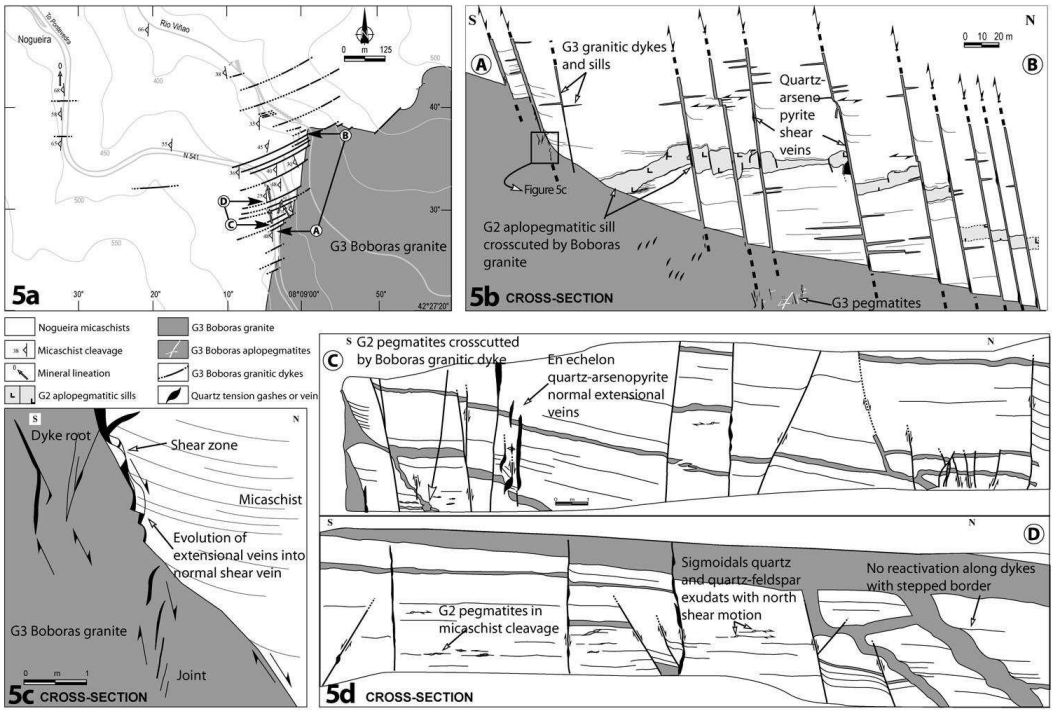

Fig. 5: (a) Geological map of the northern edge of the Boborás granite and its associated granitic dyke network. (b) Interpretative cross-section within the incised Viñao river valley of the Boborás granite roof at Brués gold deposit; cross-section drawn from field and underground mapping. (c) Detailed view of the roof geometry of the Bobóras granite showing the relationship between "en échelon" extensional veins and shear veins. (d) Cross section within micaschist on top of granite in vertical road cuts along the N541 road, which show intrusive bodies and late deformation affecting magmatic bodies.

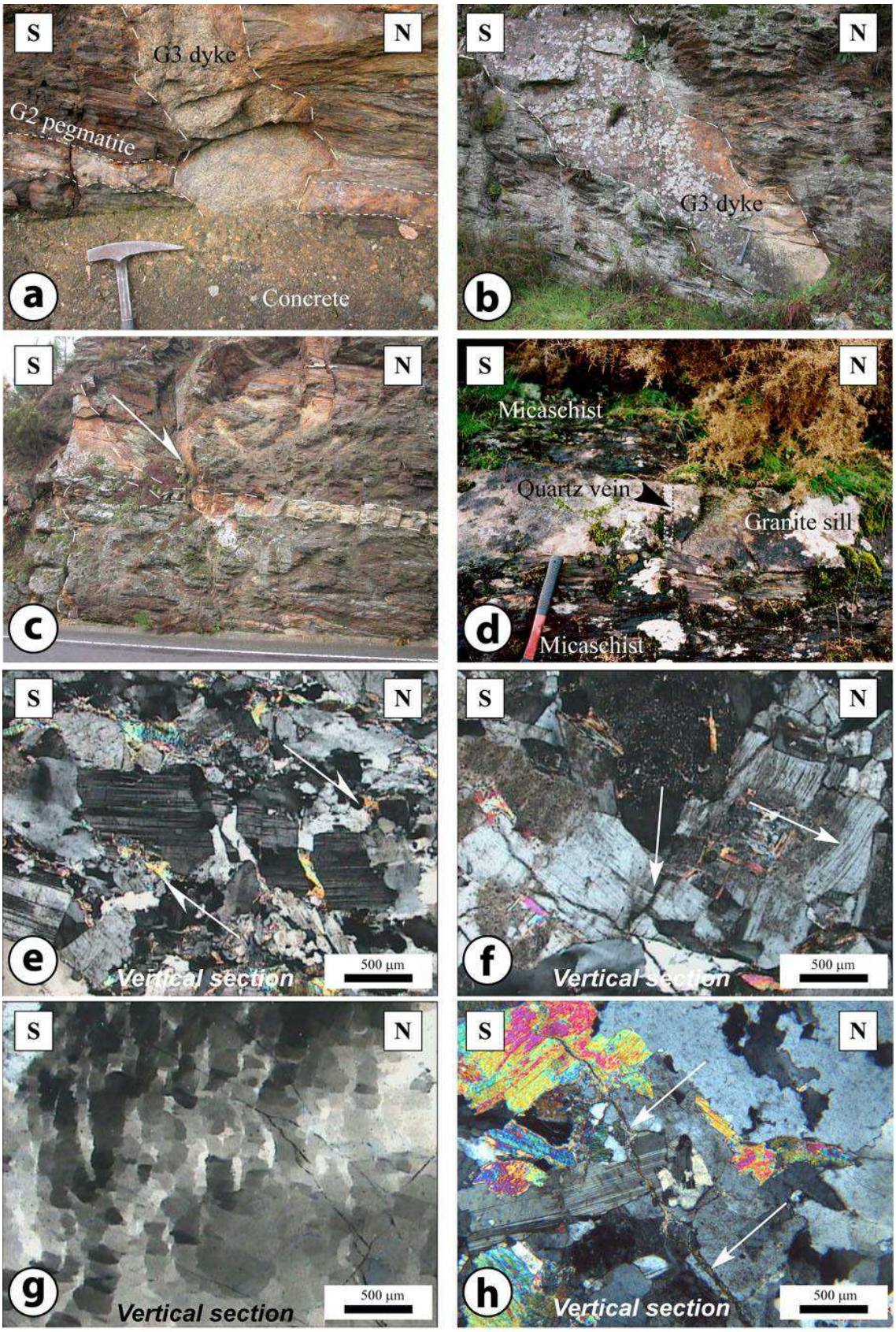

figure 6

Fig. 6: Photographs showing morphology and deformation within intrusive bodies. (a) Early

G2 pegmatite sill cross-cut by a G3 Boborás granite sill. Concrete corresponds to the upper part of the ditch of the national highway. (b) Granite dyke with staircase border consistent with north-verging shearing during granite emplacement. (c) Boborás granite dyke and sill intruding host micaschist. The shape of the connection between dyke and sill is compatible with a north-normal motion during granitic melt injection. The main schistosity is S2, and S3 is marked by a N-S horizontal lineation crenulation, not visible at this scale. (d) Stretched granite sill. The beginning of N-S boudinage (neck) is marked by a quartz extensional vein. (e) Breaking plagioclase filled by magmatic quartz showing a north-normal motion during granite dykes emplacement. (f) Plagioclases with kink bands. (g) Chessboard texture within large quartz grain from a granite dyke. (h) Solid-state fractures filled by muscovite (arrows) at the granite roof.

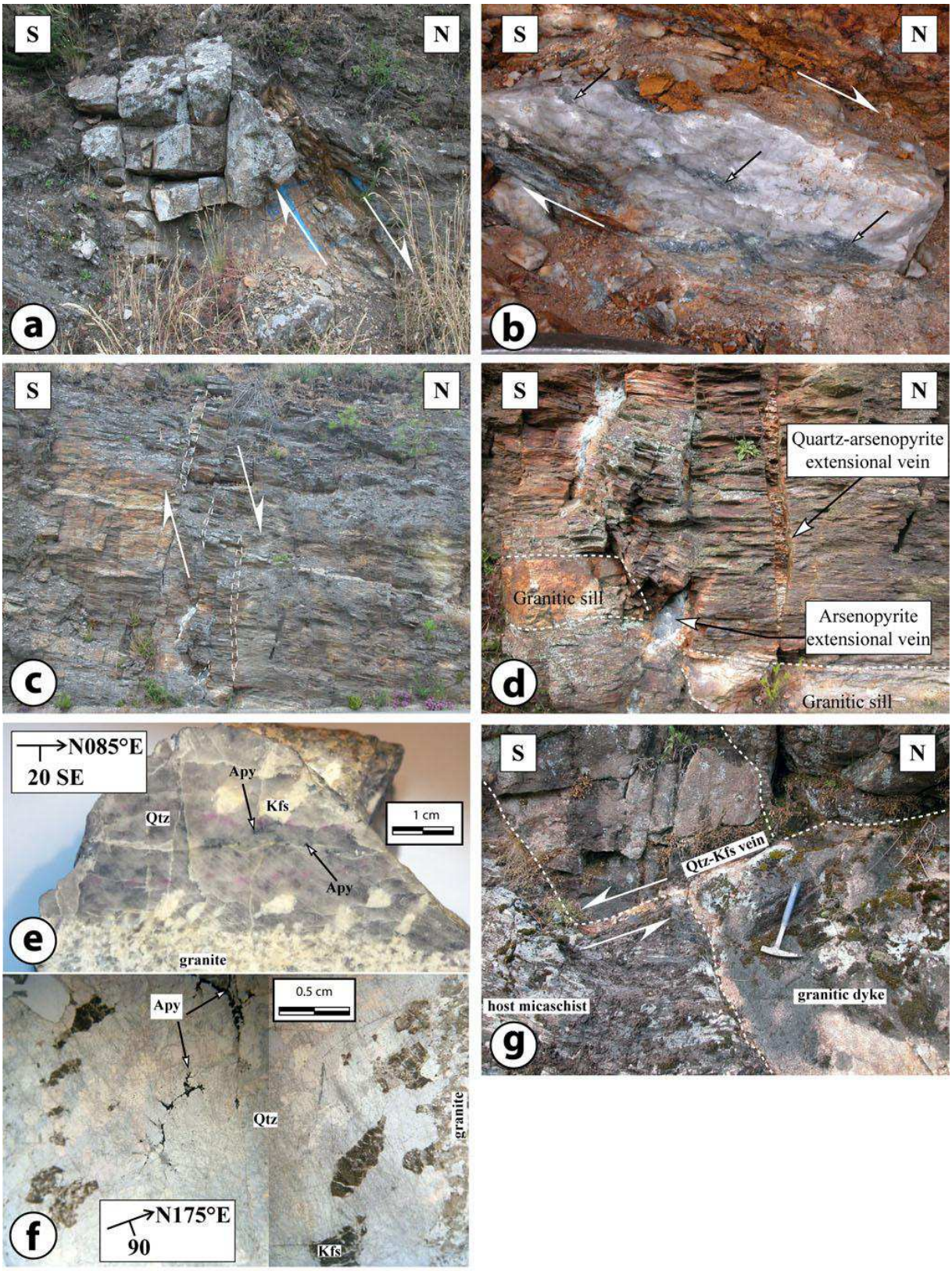

Figure 7

Fig. 7: (a) Re-used granite dyke intruding micaschist with a north-normal motion. A N088°E trending quartz-arsenopyrite shear vein dipping 60°W is emplaced within a normal fault along the dyke. (b) Detailed view of the previous photograph. Foliation in shear vein is well-marked

by arsenopyrite ribbons (located by arrows) and a N000°E trending lineation with a 60°N dip is defined by elongate quartz crystals. (c) “En échelon” quartz-arsenopyrite and arsenopyrite-bearing extensional veins compatible with a north normal motion. (d) Detailed view of the previous photograph showing the crosscutting of a granite sill by late extensional veins. (e) View of a N85°E trending quartz-feldspars vein crosscutting a granite dyke. The dip of this vein is 70° to the NW, and the section is cut perpendicular to the dip. The vein filling changes gradually from quartz-feldspar to quartz only without fractures or change in quartz morphology. This texture strongly suggests a continuum between a late-magmatic event (aplite, pegmatite) and hydrothermal events. The centre of the vein is marked by a fracture filled by a second generation of quartz and arsenopyrite. In this section the feldspar alignment suggests a dextral sense of opening. (f) View of the same vein in a vertical section. Feldspars crystals are truncated and make an angle with the vein wall; the sense of opening in a vertical section is normal toward the north. (g) View of a granite dyke crosscut by a low-angle quartz-feldspar shear vein. This movement is related to the re-use of the dyke network in a north normal faulting motion allowing emplacement of quartz veins.

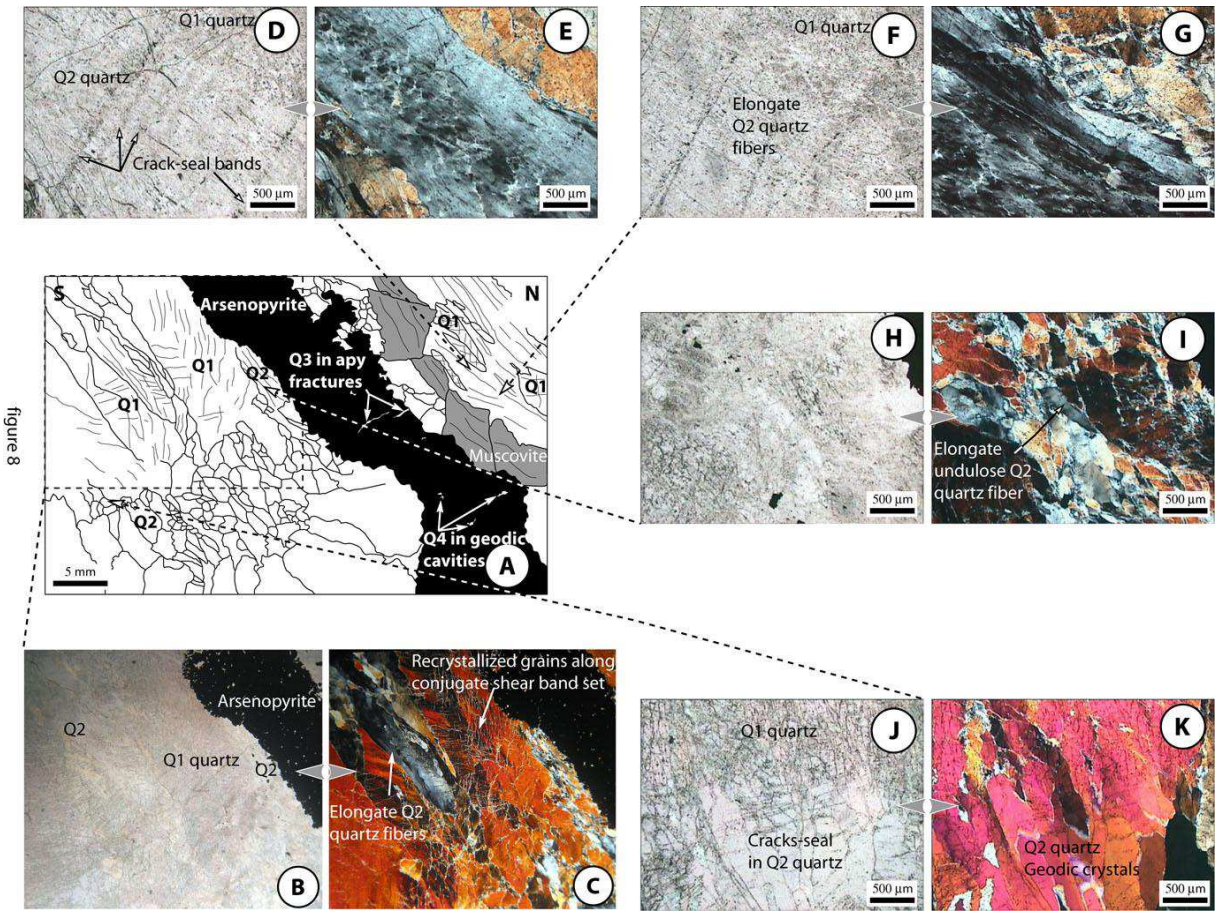

Fig. 8: Texture and filling of a north-normal quartz-arsenopyrite-bearing shear vein

crosscutting a granite dyke. (a) Typical textural association of a shear vein. Schematic illustration showing the differences in morphology and deformation of the different quartz generations. The other photographs come from this sample and are presented in transmitted light with and without crossed nicols. (b & c) View of the Q1 quartz that is dominant in volume and contains numerous conjugate shear bands of recrystallized grains. Conversely, Q2 quartz appears as wavy, clear and very elongate fibres parallel to the shear vein foliation. This foliation is underlined by a band of deformed arsenopyrite (in black). (d & e) View of part of an elongate Q2 quartz. Many crack-seals are present within this quartz and are not observed in the neighbouring Q1 quartz. Note that this fibre is affected by a beginning of shearing. (f & g) Recrystallized grains in conjugate shear bands are present in the Q1 quartz, and no crack-seal is present in this quartz. Wavy elongate quartz fibres contain crack seals. (h & i) Wavy Q2 quartz fibres appear isolated in deformed Q1 quartz, where Q2 quartz has been probably formed in a micro pull-apart structure. (j & k) Less deformed area of Q1 quartz shows the presence of a micro pull-apart structure filled by more clear Q2 quartz.

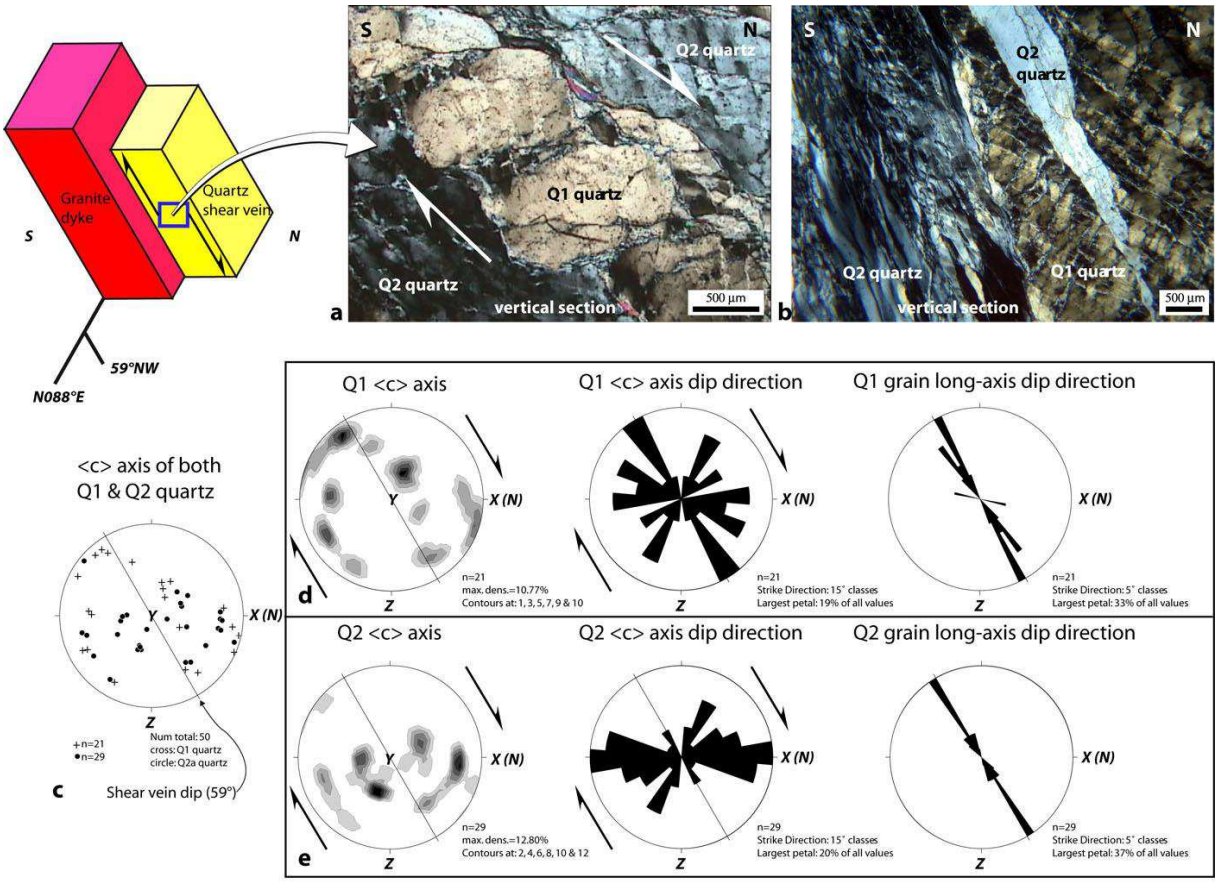

Figure 09

Fig. 9: Microstructures, [c]-axis study of Q1 and Q2 quartz generation from the north normal

shear vein shown on Fig. 7a and b. (a) Q1 quartz presents locally evidences of large rotation compatible with the sense of movement. (b) Example of quartz that has been used for the [c]-axis measurements. Q1 quartz is strongly affected by conjugate shear bands of recrystallized grains that are crosscut by Q2 strongly elongate quartz fibres. (c) [c]-axis stereograms of both Q1 and Q2 quartz. (d & e) [c]-axis stereograms, [c]-axis rose diagram strike direction and long grain axis for each quartz. Stereograms are equal area, lower hemisphere; [c]-axis diagram of Q1 quartz shows a majority of [c]-axes close to the rims of the diagram, which are normal or at high-angle with the vein border suggesting comb quartz.

However, the [c]-axis diagram of Q2 quartz shows half of the [c]-axes near the centre of the diagram. The four maxima show that [c]-axes of Q2 grains are at a high angle with the long-grain axes and that the [c]-axes dip direction is mainly to the north (X), showing an angle of about 60° with the shear vein dip compatible with Q2 as striped bedding veins form within Q1 quartz.

The differences between Q1 and Q2 quartz are compatible with a crystallization of Q2 postdating Q1, with Q2 crystallizing in opening jogs within Q1 during shearing, see details in text.

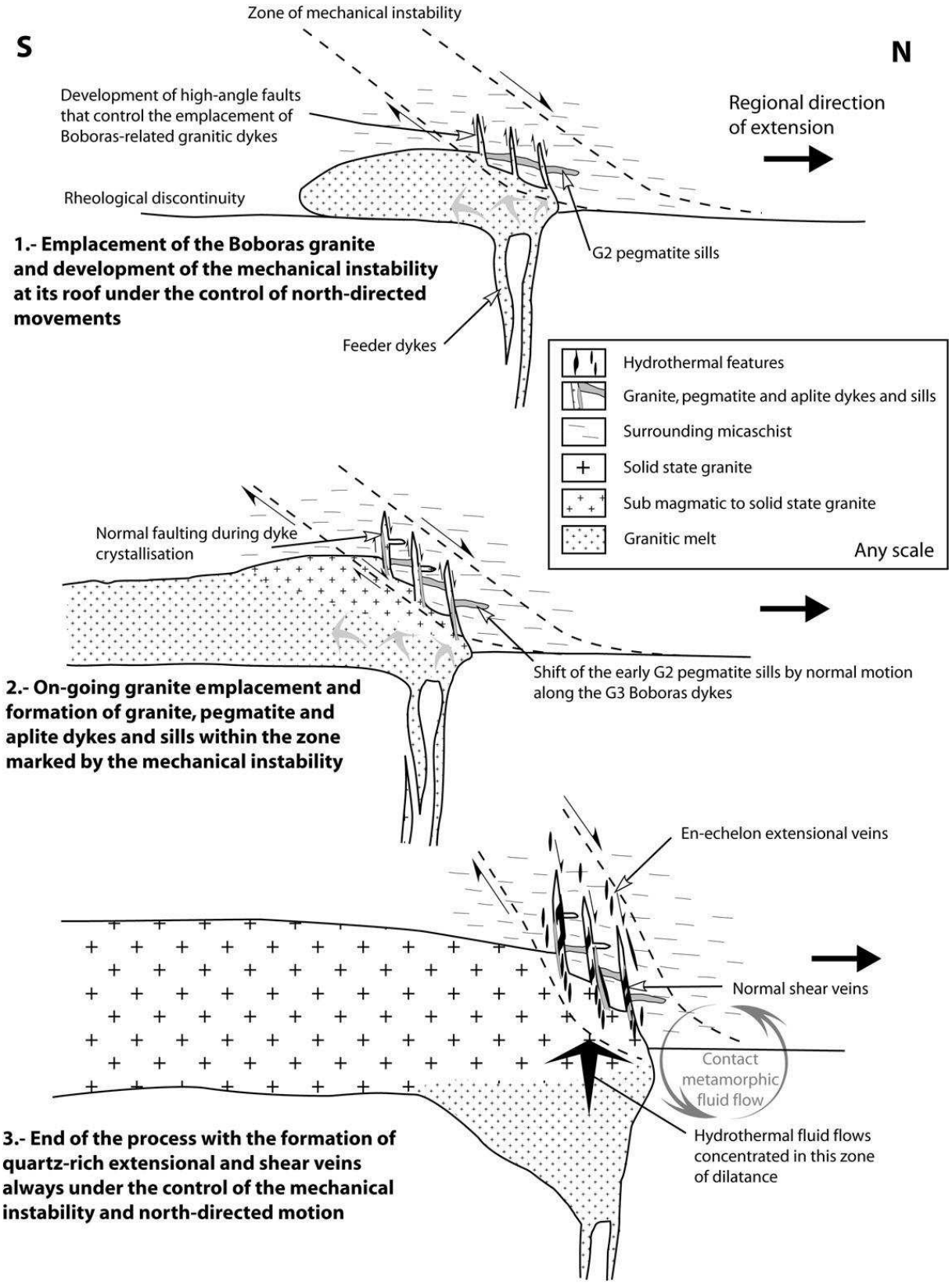

Figure 10

Fig. 10: Integrative conceptual model of the Boborás G3 granite emplacement and the associated Brués hydrothermal gold system (not to scale). (a) The first stage is the

emplacement of the G3 Bobóras granite, along a rheological discontinuity represented by the contact between the Carballiño G2 granite and micaschist. This emplacement and the location of the underlying root zone may have created a mechanical instability at the pluton's roof. Together with the regional stress, this favoured injection of the earliest granite dyke controlled by the on-going north-directed shearing. The bulk shear strain (double arrows) was very low, as attested by the lack of mylonites and detachment planes. (b) The deformation/emplacement history then continued with on-going granite and dyke emplacement, earlier emplaced granites and dykes undergoing sub-magmatic deformation. During this stage, granite sills and dykes (also affected by sub-magmatic deformation) were emplaced. (c) Vein and dyke system formation at the granite roof was achieved with the emplacement of syntectonic quartz veins, mainly close to the granite dykes and still controlled by the north-verging shearing and the mechanical instability. At this stage, many granite-dyke wall rocks were reactivated to form hydrothermal shear veins. The injection process and pluton growth increment may have continued at depth in the root zone area.